A novel ensemble method for retrieving properties of warm cloud in 3-D using ground-based scanning radar and zenith radiances

AGU PUBLICATIONS

JGR

Journal of Geophysical Research: Atmospheres

RESEARCH ARTICLE
10.1002/2014JD021742

Key Points:
- New method for retrieving 3-D cloud fields
- Three-dimensional radiative transfer is used as a forward model
- Evaluations against other retrievals show good agreement

Correspondence to:
M. D. Fielding,
m.d.fielding@pgr.reading.ac.uk

Citation:
Fielding, M. D., J. C. Chiu, R. J. Hogan, and G. Feingold (2014), A novel ensemble method for retrieving properties of warm cloud in 3-D using ground-based scanning radar and zenith radiances, *J. Geophys. Res. Atmos.*, *119*, doi:10.1002/2014JD021742.

Received 12 MAR 2014
Accepted 21 AUG 2014
Accepted article online 26 AUG 2014

A novel ensemble method for retrieving properties of warm cloud in 3-D using ground-based scanning radar and zenith radiances

Mark D. Fielding[1], J. Christine Chiu[1], Robin J. Hogan[1], and Graham Feingold[2]

[1]Department of Meteorology, University of Reading, Reading, UK, [2]NOAA Earth System Research Laboratory, Boulder, Colorado, USA

Abstract We present a novel method for retrieving high-resolution, three-dimensional (3-D) nonprecipitating cloud fields in both overcast and broken-cloud situations. The method uses scanning cloud radar and multiwavelength zenith radiances to obtain gridded 3-D liquid water content (LWC) and effective radius (r_e) and 2-D column mean droplet number concentration (N_d). By using an adaption of the ensemble Kalman filter, radiances are used to constrain the optical properties of the clouds using a forward model that employs full 3-D radiative transfer while also providing full error statistics given the uncertainty in the observations. To evaluate the new method, we first perform retrievals using synthetic measurements from a challenging cumulus cloud field produced by a large-eddy simulation snapshot. Uncertainty due to measurement error in overhead clouds is estimated at 20% in LWC and 6% in r_e, but the true error can be greater due to uncertainties in the assumed droplet size distribution and radiative transfer. Over the entire domain, LWC and r_e are retrieved with average error 0.05–0.08 g m^{-3} and ~2 μm, respectively, depending on the number of radiance channels used. The method is then evaluated using real data from the Atmospheric Radiation Measurement program Mobile Facility at the Azores. Two case studies are considered, one stratocumulus and one cumulus. Where available, the liquid water path retrieved directly above the observation site was found to be in good agreement with independent values obtained from microwave radiometer measurements, with an error of 20 g m^{-2}.

1. Introduction

Boundary layer clouds are fundamental to the Earth's radiation budget, their high reflectance constituting a significant contribution to the planetary albedo [*Hartmann et al.*, 1992]. Even small changes in their distribution or composition can have a significant effect on climate [*Oreopoulos and Platnick*, 2008]. Their turbulent, complex structures, coupled with a strong susceptibility to aerosol, mean they remain a key source of uncertainty in climate projections [e.g., *Randall et al.*, 2007; *Turner et al.*, 2007b]. To complement advances in modeling studies, accurate observations of clouds and radiation are vital to improvement in the parameterization schemes of global circulation models (GCMs).

Profiling instruments, such as vertically pointing cloud radar, are invaluable for obtaining long-term time series of clouds [e.g., *Illingworth et al.*, 2007] and give good vertical and partial horizontal information on cloud properties. However, they are less well suited for inferring a whole-sky view. This problem is particularly apparent when attempting to reproduce observed surface irradiances in radiation closure studies [*McFarlane and Evans*, 2004; *Wang et al.*, 2011] or analyzing cloud radiative effects, both of which are sorely needed as observational constraints for realistic cloud and radiation parameterizations for GCMs [*Qian et al.*, 2012]. In particular, the 3-D horizontal transport of photons (henceforth "3-D effects") is a nonnegligible source of error in the 1-D radiation schemes of current GCMs [e.g., *Cahalan et al.*, 1994; *Hogan and Shonk*, 2013], particularly for cumulus clouds [*Pincus et al.*, 2005]. The ability to observe cloud structure and cloud microphysical properties in 3-D is also a key step to improving our understanding of cloud life cycle and cloud organization.

To address this need for 3-D measurements of clouds, the U.S. Department of Energy's Atmospheric Radiation Measurement (ARM) program [*Ackerman and Stokes*, 2003] has installed scanning polarimetric Doppler cloud radar [*Widener et al.*, 2012] at their Climate Research Facilities. The radars can scan at up to 15° s^{-1} producing reasonable coverage over a 5 min time period, which can then be interpolated to a 3-D gridded domain of radar reflectivity. However, as radar reflectivity is proportional to both the number and the size of cloud droplets, further information is required to deduce these microphysical properties inside the 3-D domain.

Several existing methods to retrieve cloud microphysical properties using vertically pointing cloud radar and other sources of information could be adapted for a scanning radar retrieval. First, one could add prior knowledge based on in situ observations [e.g., *McFarlane et al*., 2002] or based on theory, for example, using a simple model to predict droplet sizes given certain atmospheric conditions [e.g., *Rémillard et al*., 2013]. Second, an additional active sensor could be added to the retrieval. For example, *Hogan et al*. [2005] and *Huang et al*. [2009] showed that differential attenuation with dual-wavelength radar could retrieve liquid water content (LWC). Finally, passive sensors could be added to the retrieval. The most widely used constraint is liquid water path (LWP) measurements from microwave radiometers [e.g., *Frisch et al*., 1995; *Frisch et al*., 1998; *Lohnert et al*., 2001]. Additionally, *Dong and Mace* [2003] combined radar measurements and cloud optical depth retrieved from solar irradiances, which works best for relatively overcast, horizontally homogeneous clouds due to the hemispheric field of view of radiometers.

In contrast to irradiances, zenith radiances are collected from a narrow field-of-view, which can capture cloud variability at higher spatial resolution and therefore are a more appealing choice for the retrieval of heterogeneous cloud. By using a wavelength that is absorbed by liquid water and one that is not absorbed by liquid water, zenith radiance measurements have previously been used to simultaneously constrain droplet size (using the absorbing wavelength) and cloud optical depth (using the nonabsorbing wavelength) without radar measurements [e.g., *McBride et al*., 2011; *Chiu et al*., 2012]. These retrievals use a plane parallel approximation; *Marshak et al*. [2004] showed that 3-D effects in heterogeneous cloud conditions can lead to "unretrievable" combinations of radiance measurements. The greater the heterogeneity in the cloud field, the greater the 3-D effects, which increases the potential for error in both the retrieved microphysical and radiative properties of the cloud.

As scanning cloud radar provides information on the 3-D cloud structure, it appears possible to utilize these formerly unwelcome 3-D effects, provided that 3-D radiative transfer is used as a forward model. A potential stumbling block is that modeling 3-D radiative transfer is a difficult problem and typically their adjoints (models that specify the sensitivity of their output to their input) do not exist, which rules out many standard techniques for solving inverse problems. By using an ensemble-based method, we will show that we can overcome this issue and use 3-D effects to our advantage.

In this paper, we propose a novel ENsemble ClOud REtrieval method (ENCORE) to retrieve the 3-D microphysical properties of clouds using scanning cloud radar and zenith radiances. The method has three key features. First, by using an ensemble-based method, we can use full 3-D radiative transfer as a forward model without the need for its adjoint. As far as we are aware, the only previous use of a similar method for a meteorological radar retrieval is that described by *Grecu and Olson* [2008]. Second, while satellite-based radiance-radar retrievals have been developed for CloudSat and Moderate Resolution Imaging Spectroradiometer (MODIS) [*Austin and Stephens*, 2001], we are unaware of an equivalent ground-based method. Finally, the retrieval is independent of microwave-based LWP retrievals, permitting their use for validation.

The paper is organized as follows. We present the methodology of our 3-D retrieval for nonprecipitating boundary layer clouds in section 2. In section 3 we evaluate the retrieval using synthetic cloud fields from large-eddy simulations. Section 4 contains an analysis of two case study retrievals, one for a cumulus cloud field and one for a stratocumulus cloud field. A discussion follows in section 5, and the conclusions and summary are in section 6.

2. Methodology of ENCORE

2.1. Overview of Retrieval Method

The method retrieves 2-D fields of cloud droplet number concentration N_d (assumed constant with height) and 3-D LWC and r_e. Our retrieval is built on a flexible ensemble framework that allows for the easy addition or removal of any observational data set. In this paper, the framework is used to maximize the synergy between zenith radiances and radar reflectivity from scanning radar.

The required observational data sets are available from colocated instruments at various ARM field sites. Ground-based scanning ARM cloud radars (SACRs) provide radar reflectivity [*Widener et al*., 2012]. At each field site, two radars of different frequency are mounted onto a single pedestal, typically Ka and W band. Both these radars have very narrow fields of view (~0.3°) making them ideal for cloud studies [*Kollias et al*., 2014].

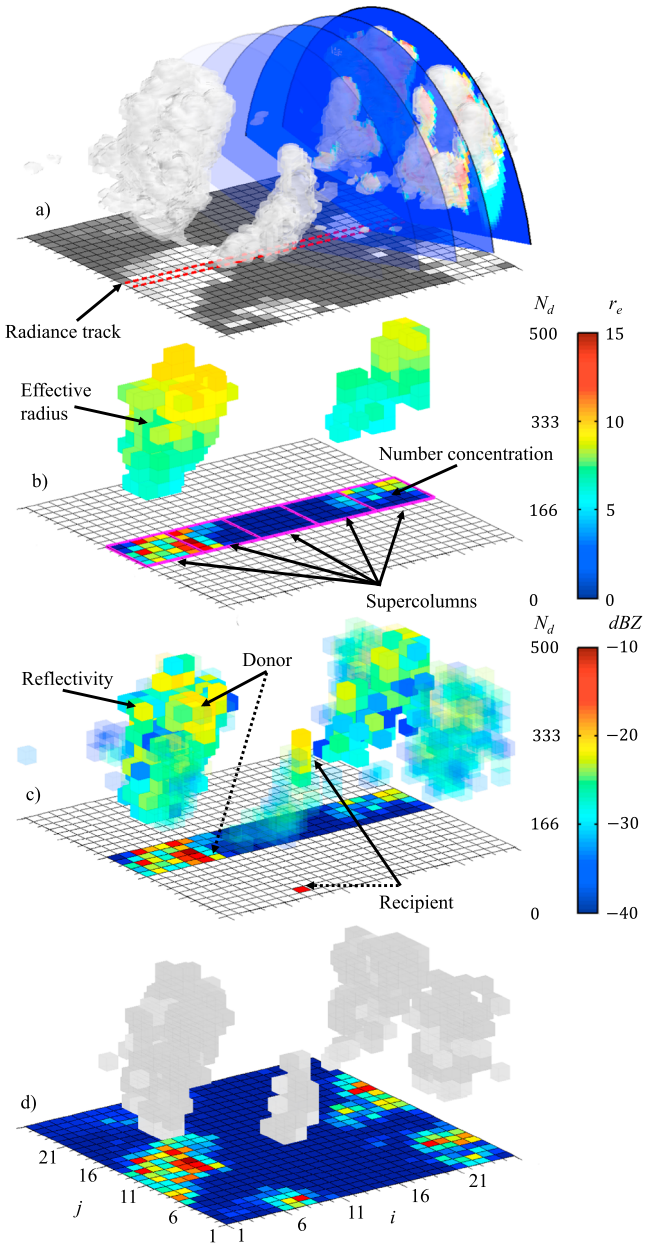

Figure 1. Diagram showing the main steps of the ENsemble ClOud REtrieval method (ENCORE). (a) Gathering of radiance (red dashed lines) and radar reflectivity (hemispherical slices) observations, (b) retrieved drop number concentration and effective radius within each supercolumn (magenta boxes), (c) reflectivity matching of donor columns (solid) to recipient columns (translucent), and (d) completed retrieval.

Zenith radiance measurements are available from ARM narrow field of view radiometers (2NFOV) or ARM shortwave array spectroradiometers (SAS-Ze). Both of these instruments are ground based with 1 s temporal resolution. The 2NFOV has channels at 673 and 870 nm with a 1.2° field of view. The SAS-Ze measures radiances across the whole shortwave spectrum (350–1700 nm) at a spectral resolution of 2.4 nm in the visible and 6 nm in the near infrared with a 1° field-of-view. For clarity, in the rest of the paper we will refer to wavelengths of radiation that are absorbed by liquid water as "absorbing" (e.g., 1640 nm) and those that are not as "nonabsorbing" (e.g., 440, 673, and 870 nm). Since the zenith radiances are local column-averaged measurements and do not provide detailed cloud information for the full 3-D domain, our retrieval procedure contains three major steps, as illustrated in Figure 1 and outlined next.

The first step is to place all observations on to a common grid. Scanning radar observations are mapped to a regular 3-D grid, using linear interpolation via a Delaunay triangulation [see *Fielding et al.*, 2013]. Figure 1a illustrates an example of radar scans made with the Cross Wind Range Height Indicator (CWRHI) strategy from a radar located in the center of the domain. Similarly, zenith radiance observations are also collected at the center of the domain and are linearly interpolated to a 1-D track. Both data sets are placed on a spatial grid by assuming the commonly used frozen turbulence hypothesis, with wind speed and direction obtained from a colocated wind profiler.

Each zenith radiance observation is mainly a function of the overhead cloud properties due to the narrow field of view of the radiometers; however, when 3-D effects are not negligible, 1-D radiative transfer calculations are insufficient to satisfactorily simulate zenith radiances and thus cannot provide proper constraints for our retrievals. Therefore, 3-D radiative transfer calculations need to be incorporated in our algorithm. Due to the trade-off between computational cost and the inclusion of 3-D effects, the second step of the retrieval is restricted to a series of subsets of the full domain; each subset domain, dubbed a "supercolumn," is selected along the aforementioned 1-D "radiance" track. The size of the supercolumn (magenta squares in Figure 1b) is chosen to reduce computational cost while encompassing most 3-D effects. This second step is a key component of our retrieval method and will be detailed in section 2.2.

Once the retrievals for the supercolumns are complete, the third step, illustrated in Figure 1c, is to retrieve cloud properties for the rest of the domain by matching their radar reflectivity with the clouds inside the supercolumns. Details are given in section 2.3.

2.2. Retrieval for Supercolumns

2.2.1. State Vector and Forward Models

The state vector, **x**, which contains the variables we wish to retrieve, is defined as

$$\mathbf{x} = \left(\log N_{\mathrm{d}}^{(i=1\ldots m,\ j=1\ldots n)},\ \log r_e^{(i=1\ldots m,\ j=1\ldots n,\ k=1\ldots l)} \right)^T, \tag{1}$$

where i and j are grid indices in the horizontal; k is the vertical index; and n, m, and l define the number of horizontal and vertical grid points in the supercolumn, respectively. The variables in **x** are defined in log space to keep their values positive in linear space. Cloud droplet number concentration N_{d} is forced to be height invariant, whereas r_{e} is allowed to vary with height. LWC is defined as

$$\mathrm{LWC} = \frac{4}{3}\pi\rho_w\, N_{\mathrm{d}} r_{\mathrm{e}}^3\, \exp\left(-3\sigma^2\right), \tag{2}$$

where σ is the shape parameter or geometric standard deviation (standard deviation of the log of droplet radius), and ρ_w is the density of liquid water. As σ is not retrieved, we choose to keep it constant; we discuss the impact of this assumption on retrievals in section 3.3. From LWC and r_{e}, cloud optical depth, τ, can be given as

$$\tau = \frac{3}{2\rho_w}\int_{H_B}^{H_T} \frac{\mathrm{LWC}(h)}{r_{\mathrm{e}}(h)}\,\mathrm{d}h, \tag{3}$$

where H_{B} is the height of cloud base and H_{T} is the cloud top and the extinction efficiency has been assumed to be 2 (valid in the visible part of the spectrum).

Using N_{d}, r_{e}, and a lognormal cloud droplet distribution, we can also now forward model radar reflectivity and zenith radiance, needed to map the state variables to observation space. We can safely use the Rayleigh scattering approximation for cloud droplets since the SACRs operate at Ka or W band, but at these high frequencies we must account for gas and liquid water attenuation. As a result, radar reflectivity is given as

$$Z = \frac{64 N_{\mathrm{d}} r_{\mathrm{e}}^6 \exp(3\sigma^2)}{10^{0.2\int_0^L (\alpha_f + \kappa_f \cdot \mathrm{LWC})\ \mathrm{d}L'}}, \tag{4}$$

where α_f (dB km^{-1}) is the one-way specific attenuation coefficient due to atmospheric gases, κ_f (dB km^{-1} (g m^{-3})$^{-1}$) is the one-way specific attenuation coefficient of liquid water [*Hogan et al.*, 2005], and L is the distance to the radar. Note that the assumed unimodal lognormal droplet distribution is only suitable for nonprecipitating clouds. Indeed, the success of the retrieval is strongly dependent on the validity of our assumed droplet distribution; we are inferring the zeroth, second, and third moments from observations of the second and sixth moments.

Zenith radiances are computed using fully 3-D radiative transfer. The effective radius from the state vector and LWC determined from equation (2) are used to determine cloud extinction, single-scattering albedo, and phase function. To interpret real observations, these need to be combined with similar properties for aerosols and gases, but since absorption is small at the wavelengths considered, we ignore gaseous attenuation. Aerosol properties are not included in the large-eddy simulations (LES) experiments. Radiative transfer is computed using the Spherical Harmonics Discrete Ordinated Method [*Evans*, 1998]. The surface albedo is specified using estimates from MODIS operational products [*Schaaf et al.*, 2002].

2.2.2. Finding the Best Estimate of the State Vector

To find the best estimate of the state vector, we use an adaption to the ensemble Kalman filter (EnKF, see *Evensen* [2003]) similar to *Grecu and Olson* [2008] and *Iglesias et al.* [2013]. We outline the theoretical basis first and then use Figure 2 to explain the practical details.

Let us define an ensemble **X** of individual state vectors, **x**, containing N members, i.e.,

$$\mathbf{X} = (\mathbf{x}_1, \ldots, \mathbf{x}_N), \tag{5}$$

where the subscript refers to the particular ensemble member. The mean of **X** represents the best estimate of the state vector, and the spread of the ensemble members around the mean represents the uncertainty in

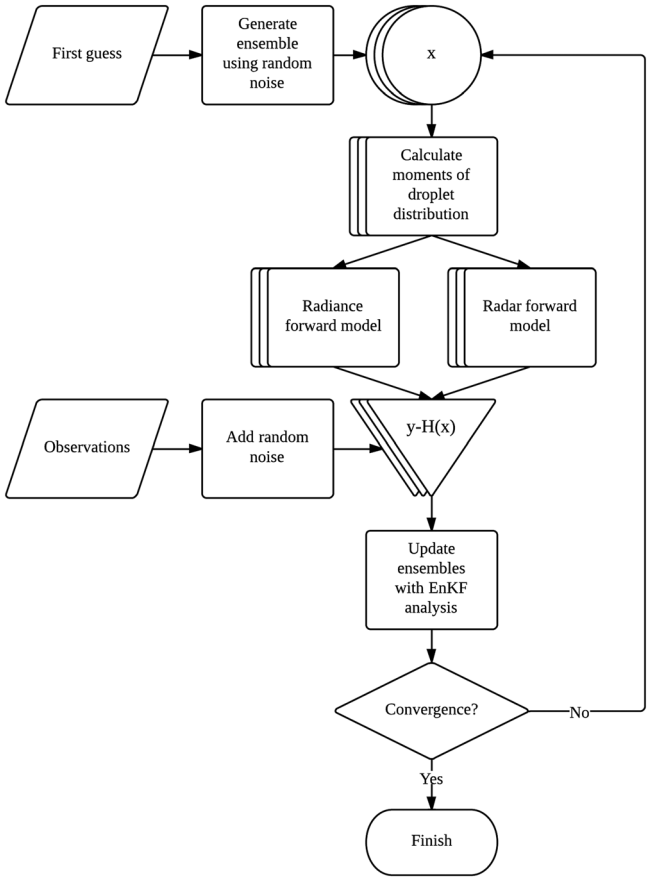

Figure 2. Flowchart describing the ensemble state estimation method.

the best estimate. For each set of observations **y**, the ensemble is updated (subscript "new") from the current estimate of the state (subscript "old") by applying the Extended Kalman Filter update equations [*Gelb*, 1974], to each ensemble member q, i.e.,

$$\mathbf{x}_{q,\text{new}} = \mathbf{x}_{q,\text{old}} + \mathbf{K}\left(\hat{\mathbf{y}}_q - H\left(\mathbf{x}_{q,\text{old}}\right)\right), \text{ and} \tag{6}$$

$$\mathbf{K} = \mathbf{P}\mathbf{C}^T\left(\mathbf{C}\mathbf{P}\mathbf{C}^T + \mathbf{R}\right)^{-1}, \tag{7}$$

where the function $H(\mathbf{x})$ is the forward model; **C** is the Jacobian of the forward model and is the sensitivity of the forward model to its input; **P** is the error covariance matrix of the current state; **R** is the observation error covariance matrix, which represents the uncertainty in the observations; and $\hat{\mathbf{y}}$ represents the observations perturbed with random noise with variance specified by **R**. **K**, known as the Kalman gain matrix, controls how much weight is placed on the observations compared to the current state. As we do not know **C** for a 3-D radiative transfer forward model, we approximate **K** via the ensemble as follows:

$$\mathbf{E}_x = \left[\mathbf{x}_1 - \overline{\mathbf{X}}, \cdots, \mathbf{x}_N - \overline{\mathbf{X}}\right] \tag{8}$$

$$\mathbf{E}_y = \left[H(\mathbf{x}_1) - \overline{H(\mathbf{x})}, \cdots, H(\mathbf{x}_N) - \overline{H(\mathbf{x})}\right], \tag{9}$$

where $\mathbf{E}_x$ represents the ensemble spread, $\mathbf{E}_y$ represents the spread in predicted observation values, and $\overline{H(\mathbf{x})}$ is the mean of the forward modeled observations. We then use

$$\mathbf{P}\mathbf{C}^T \cong \frac{1}{N-1}\mathbf{E}_x\left(\mathbf{E}_y\right)^T, \text{ and} \tag{10}$$

$$\mathbf{C}\mathbf{P}\mathbf{C}^T \cong \frac{1}{N-1}\mathbf{E}_y\left(\mathbf{E}_y\right)^T, \tag{11}$$

so that **C** is not required (see *Gillijns et al*. [2006] for a full derivation). Equation (10) can therefore be thought of as the covariance between the error in the estimate of the state and the error in the predicted observations and equation (11) as the covariance of the error in the predicted observations.

In the standard EnKF, equations (6) and (7) would be calculated once per set of observations to provide an estimate of the state that is an error-weighted combination of the current state and observations. In our adaptation, instead of sequentially updating our state at each set of observations, we iterate equations (6)–(11) using the same observations until the forward modeled values fit the observations to a specified tolerance, effectively losing the information of the state at the start of the iterative process. Note that the reuse of observations introduces correlations between the error in the state and the error in the observations, potentially introducing additional error to the retrieval [*Ide et al*., 1997]. However, in agreement with *Yang et al*. [2012], we found no significant decrease in error when introducing new, independent observation errors at every new iteration when testing the method with synthetic data, although there was a tendency for an increase in the ensemble spread. We also add a small amount of additional noise after each iteration to help explore the state space, which also helps to reduce any error introduced by reusing observations. Nevertheless, caution should be exercised when using the ensemble spread to estimate the uncertainty in the retrieval.

The details of the method are outlined in Figure 2. First, an initial ensemble, **X**, of state variables is generated from a first guess by perturbing each member with random noise with their spread representing **P**. The first guess is chosen from the climatological mean. For a sufficiently large initial uncertainty (**P**) and a large number of iterations, the choice of the first guess has little influence on the final solution, because the information of the first guess gets lost during iterations as discussed above. Once the ensemble has been set up, the iterative procedure begins. Each ensemble member is forward modeled according to the observations available. To ensure the correct ensemble spread is maintained, each ensemble member "sees" a slightly different set of observations (i.e., $\hat{\mathbf{y}}$) by adding random error to each observation according to **R**. The $\hat{\mathbf{y}}$ is generated with a new set of random errors at each iteration. Errors in the forward model can also be included in **R** by adding noise to the appropriate parameter (e.g., surface albedo in the radiance forward model). Next, the EnKF update step is calculated using equations (6)–(11). The procedure is iterated by setting $\mathbf{x}_{q,\mathrm{old}}$ equal to $\mathbf{x}_{q,\mathrm{new}}$ until convergence between the observations **y** and the forward modeled values, $\overline{H(\mathbf{x})}$. For each new set of observations, a new ensemble is generated so that each retrieval is independent.

We use the measurement uncertainties of the SACR, 2NFOV, and SAS-Ze to specify the observation error covariance matrix **R**. We assume the errors are unbiased, Gaussian, and uncorrelated between different radar gates and radiance channels. Random measurement error in radar is caused by the fluctuating constructive and destructive interference from the backscatter of the cloud droplets moving relative to each other inside the target volume. The magnitude of this error is a function of the number of independent samples and the signal-to-noise ratio, both of which are deducible from SACR measurements. For the experiments with synthetic measurements, we assume a constant random measurement error of 2 dB. We assume a 5% measurement uncertainty in zenith radiances [*Holben et al*., 1998], a 10% uncertainty in surface albedo for 440 nm wavelength, and 5% uncertainty for all other wavelengths [*Schaaf et al*., 2002].

In the experiments here, we make an adaption to the method to save computational cost. *Evensen and VanLeeuwen* [1996] recommended that the number of ensemble members should equal the size of the state. The computational cost of an ensemble size that matched the number of grid points in a supercolumn would be prohibitively expensive; following *Hogan* [2007], we therefore reduce the size of the state by assuming that r_e is perfectly defined by Z and the column mean N_d (i.e., rearranging equation (4) so r_e is in terms of Z and N_d). Random measurement error can still be accounted for in the radar reflectivity by adding the appropriate noise to Z when calculating r_e and LWC for the radiance forward model. This allows us to simplify equation (1) so that the state vector only contains a 2-D array of column mean N_d.

2.3. Retrieval for the Rest of the Domain (Outside Supercolumns)

Once the supercolumns have been independently retrieved, cloud information for the rest of the domain is retrieved by matching their radar reflectivity factor with those in the supercolumns as follows: We define columns inside the supercolumn as donor columns and those outside the supercolumns as recipient

columns, following a method similar to *Barker et al.* [2011]. For each recipient column, we choose a donor column with the least sum of the squared differences in radar reflectivity between donor and recipient, i.e.,

$$\underset{\mathrm{dBZ}_{\mathrm{donor}}\in Y}{\operatorname{argmin}} \sum_{k=H_B}^{H_T} \left(\mathrm{dBZ}^k_{\mathrm{recip}} - \mathrm{dBZ}^k_{\mathrm{donor}}\right)^2, \tag{12}$$

where Y is a set containing all the columns inside the supercolumns. Then, we assign the N_d of the closest-matching donor column to the recipient column and further retrieve r_e and LWC using the recipient column's reflectivity and equations (4) and (2). The process is repeated for all recipient columns.

Note that it would be possible to assign a different moment of the droplet distribution (e.g., r_e) to the columns of similar Z. However, this would likely cause N_d to vary significantly and unrealistically with space. We therefore choose to assign N_d to maintain consistency with the supercolumns.

3. Evaluations Using Synthetic Measurements From Large-Eddy Simulations

We evaluate the retrieval method using a selection of snapshots of shallow trade wind cumulus generated by a LES model with forcing data collected from the Rain In Cumulus over Ocean campaign [*Jiang et al.*, 2009]. The original domain size is $6.4 \times 6.4 \times 4$ km with grid spacing $25 \times 25 \times 10$ m and horizontally periodic boundary conditions but is reduced to $50 \times 50 \times 50$ m grid spacing to simulate the resolution of a gridded scanning radar reflectivity field. To ensure a nonprecipitating cloud field, snapshots are taken from a simulation initialized with 1000 cm^{-3} hygroscopic aerosol particles, only some fraction of which is activated. The snapshots contain a range of cloud sizes in both area and depth, with cloud average LWP of 37 $\mathrm{g\,m}^{-2}$ (a maximum of 400 $\mathrm{g\,m}^{-2}$) and r_e typically less than 10 μm. Cloud fraction is on the order of 10%.

Truth cloud microphysical properties are calculated directly from the droplet size distributions of the LES, sorted into 33 size bins. Thus, moments of the droplet size distribution such as Z or τ are calculated without assuming a basis function for the size distribution. However, as N_d is an intensive variable, it is not obvious how to calculate the truth column average N_d to compare with the retrieved N_d. As our retrieval is constrained with radiances, we use an extinction-weighted effective number concentration, N_{eff}, calculated from the LES snapshot using the visible extinction, σ_{ext}, and number concentration calculated at each height level, k:

$$N_{\mathrm{eff}} = \frac{\sum_{k=1}^{l} N_{\mathrm{d},k} \cdot \sigma_{\mathrm{ext},\,k}}{\sum_{k=1}^{l} \sigma_{\mathrm{ext},\,k}}, \tag{13}$$

where l is the total number of levels in the snapshot.

3.1. Experiment Setup

Each retrieval uses a snapshot in time of the entire model domain. Synthetic observations of radiances are calculated using 3-D radiative transfer across the whole domain at 673 and 870 nm to mimic 2NFOV observations and 440, 870, and 1640 nm to mimic SAS-Ze observations. The radiances are calculated along a 1-D track across the domain, collocated with the supercolumns.

Synthetic observations of gridded radar reflectivity are created directly from the LES. The radar reflectivity is calculated directly from the droplet distributions using a Rayleigh scattering approximation. To limit the source of errors in the retrieval method, we do not account for errors in gridding the data or errors due to gaseous or liquid water attenuation. While we assume an infinitely sensitive radar in the supercolumn retrieval stage, we do restrict the reflectivity in the extrapolation stage to points greater than -50 dBZ so only cloud grid points are included in the minimization of equation (12).

As mentioned in section 2.2, retrievals are performed for supercolumns first, and the size of the supercolumns should be optimized to account for as much as possible of the 3-D effects in radiance measurements while having an acceptable computational time. To find the optimal domain size required to accurately forward model radiances, we compared radiances calculated by 3-D radiative transfer using smaller subdomains to a LES cumulus snapshot "truth" with zenith radiances calculated using the whole domain. As expected, we found that the root-mean-square error (RMSE) and the bias in the radiances generally decreased with increasing supercolumn size. To accurately forward model radiances with an RMSE of less than 10%, the

Table 1. First Guesses and Uncertainties for Experiments With Synthetic Data

Parameter/Observation	Mean Value	Standard Deviation
Cloud droplet number concentration N_d (cm^{-3})	100	50
Lognormal shape parameter (unitless)	0.3	0.05
Zenith radiance ($W\,m^{-2}\,\mu m^{-1}\,nm^{-1}\,sr^{-1}$)	Calculated from 3-D radiative transfer given a cloud field	5%
Surface albedo		
440 nm and 673 nm	0.05	10%
870 nm	0.3	5%
1640 nm	0.25	5%
Radar Reflectivity (dBZ)	Calculated directly from LES snapshot	2

supercolumn width must be around 1500 m for solar zenith angle (SZA) of 30° and 2500 m for SZA of 60° (figures not shown).

Ideally, we would simply use a supercolumn with a width of 2500 m or larger. However, given a high spatial resolution retrieval, this would create a large state vector such that the retrieval method would require a computationally prohibitive number of ensemble members. As a compromise, we nest the supercolumn inside a "buffer zone" that is not explicitly retrieved but used in the radiative transfer forward model. We can do this by calculating LWC and r_e using Z and the first guess of N_d (again, rearranging equation (4) so r_e is in terms of Z).

Table 1 lists the key input parameters and settings for the evaluation experiments. We set the supercolumn to contain 5×5 columns, giving a total width of 250 m and a total state size of 25. The vertical resolution is 50 m. Each supercolumn is nested inside a buffer zone with width 1500 m for a 30° SZA. The shape parameter σ was chosen such that it minimized the RMSE between the true LWC from the LES data and the LWC derived from equation (2) using the true N_d and r_e from the LES data. This gave a value of 0.3, which is consistent with shape parameters from in situ observations in *Miles et al*. [2000]. The first guess for each N_d assigned to each ensemble member was chosen to be $100\,cm^{-3}$, close to the cloud average N_d in the snapshot. Random noise with standard deviation of $\sim 50\,cm^{-3}$ is added to each ensemble member in log space.

3.2. Evaluation Results

Figure 3 shows domain retrievals from a single case using synthetic SACR reflectivity and SAS-Ze zenith radiances at 440, 870, and 1640 nm. Qualitatively, the retrievals well capture areas of cloud with higher N_d; the spatial distribution and the magnitude of r_e are also reasonable. Consequently, the retrieved LWP is very similar to the truth except at cloud edges where radar reflectivity is less than −50 dBZ, which excludes them from the donor-recipient process of the retrieval (i.e., step 3 in section 2.1).

To focus on quantitative evaluations over cloudy regions only, we define a cloudy column as a region with LWP greater than $5\,g\,m^{-2}$ and a cloudy voxel where LWC is greater than $0.01\,g\,m^{-3}$. Table 2 shows that the truth has a domain average LWP of $37\,g\,m^{-2}$, r_e of 6.4 μm, and N_d of $196\,cm^{-3}$ over cloudy columns. Whole domain retrievals in Figure 3 have a mean LWP remarkably close to the truth mean, but the corresponding RMSE is $19\,g\,m^{-2}$. Not surprisingly, similar error characteristics with a slightly negative bias and a relatively large RMSE are also found in LWC retrievals over cloudy voxels. Additionally, retrieved r_e in cloudy voxels have a negative bias of 19% and RMSE of 2 μm, which leads to a positive bias in τ of ~1 over cloudy columns.

We now look more carefully at the errors in the supercolumns where the heart of our retrieval method is performed. Figure 4 compares retrieved column-averaged properties with the truth along the radiance track. This cross section is a good test for the retrieval—it contains optically thin cumulus clouds with reflectivities below −40 dBZ to the left of the domain and a much deeper, developed cloud toward the right with a core of −20 dBZ. Retrieved N_d is generally close to the truth except for the very thin clouds at the start of the cross section. LWP and τ match well and have correlations above 0.9. Effective radius is slightly underestimated, especially where N_d is overestimated at the start of the cross section. The radiance becomes very sensitive to N_d in low reflectivity clouds, as shown by the larger uncertainty (blue shading in Figure 4b). Overall, the average uncertainty is 77% in N_d, which translates to a 20% uncertainty in LWC and 6% uncertainty in r_e calculated via equations (2) and (4). If the retrieval were to be used as an operational product, retrievals associated with large uncertainty in N_d could be flagged as potentially unreliable to prevent misleading results. Also, a very thin cloud might not conform to a lognormal droplet distribution with an assumed shape

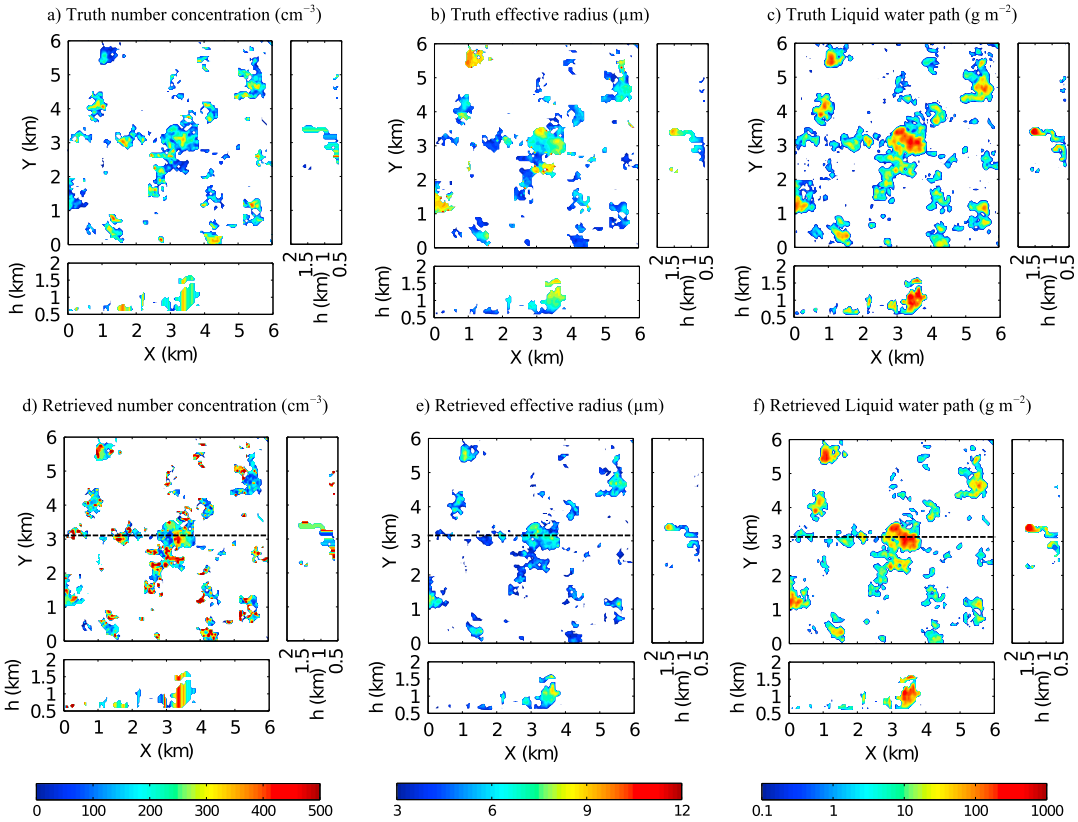

Figure 3. Truth LES snapshot (top row) and retrieved (bottom row) column-averaged (main panels) and vertical cross sections (side panels; bottom, $Y = 3.1$ km, right, $X = 3.1$ km) of number concentration, effective radius, and liquid water path. The retrieval used synthetic radiances at 440, 870, and 1640 nm and synthetic radar measurements, with SZA = 30° and parameters as given in Table 1. The black dashed line indicates the track of radiance measurements. The sun angle is in the positive Y direction.

parameter of 0.3. Overestimating the shape parameter would lead to an underestimation of r_e, as discussed in section 3.3.2.

We can also consider individual profiles in the domain. Figure 5 shows the vertical profile of N_d, LWC, and r_e in the core of the large cloud at $X = 3$ km and $Y = 3$ km. Each cloud property matches well with the truth. Above 1400 m there is a second layer of cloud with larger r_e yet smaller N_d than the cloud below. This is presumably because it is the remnants of a larger cloud where all the smaller droplets have evaporated as a result of dry air entrained in to the cloud. As the retrieval is constrained to a constant N_d with height, the N_d in the lower cloud is slightly underestimated, while the upper cloud N_d is overestimated. The nonlinearity

Table 2. Average Cloud Properties in Cloudy Regions[a] Across the Full Domain and Within the Supercolumns Only for the Truth and Retrieval

	LWC (g m^{-3})	r_e (μm)	LWP (g m^{-2})	N_d (cm^{-3})[b]	τ
Full domain					
Truth	0.113	6.4	37.37	196	8.1
Retrieval	0.112	5.2	36.41	258	8.5
Supercolumns					
Truth	0.165	6.5	72.82	220	15.3
Retrieval	0.160	5.7	71.48	262	16.3

[a]Defined as cloudy voxels greater than 0.01 g m^{-3} and columns with LWP greater than 5 g m^{-2}.
[b]Droplet number concentration for the truth is calculated using equation (13).

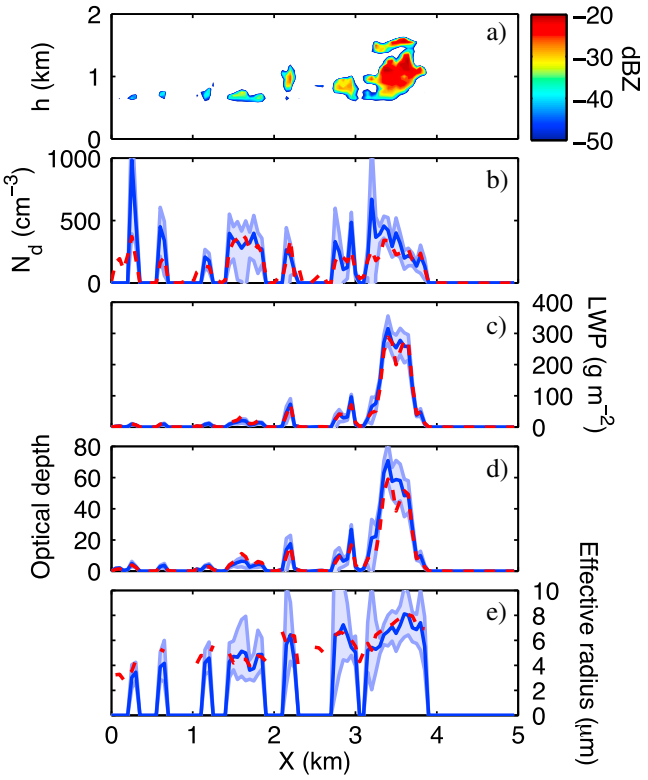

Figure 4. Retrieved cloud properties along the track of radiances at $Y = 3.1$ km, using synthetic data shown in Figure 3. (a) Radar reflectivity, (b) cloud droplet number concentration (N_d), (c) liquid water path (LWP), (d) optical depth, and (e) effective radius. Retrieved values are shown in dark blue with uncertainty of one standard deviation uncertainty in light blue shading, while the corresponding truth values are represented by the dashed red lines.

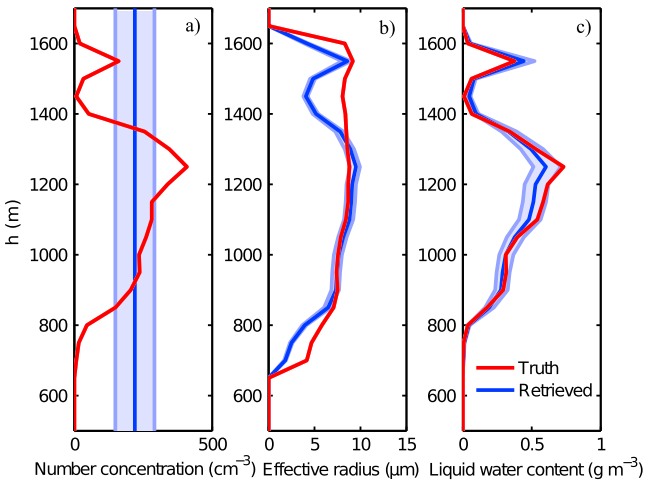

Figure 5. The truth (red; from LES in this case) and retrieved (blue) vertical profiles of (a) cloud droplet number concentration, (b) cloud effective radius, and (c) LWC, taken from $X = 3$ km, $Y = 3$ km in Figure 3. Retrievals are plotted with one standard deviation (shaded light blue) estimated from the spread of the ensembles.

between different parameters causes a difference in the size of the uncertainty, with N_d most uncertain and r_e the least uncertain. The true uncertainties are likely to be greater, as discussed in the next section.

To summarize, within the supercolumns, r_e is underestimated by 12% and N_d is overestimated by 20%, primarily due to the thin clouds at the start of the section. Biases in LWC and LWP are less (around 3%) as most of the contribution to the average is from the thicker clouds at the end of the section. Note that when changing the first guess N_d between 50 and 500 cm^{-3}, retrieval biases are similar and vary by only 5% for both LWP and r_e.

3.3. Sensitivity of Retrieval to Radiance Wavelength and Droplet Distribution

A number of factors potentially affect the retrieval and its uncertainty, including the choice of wavelength in radiance measurements and the lognormal droplet distribution assumption. Using the same LES cumulus snapshot, the impact of each factor on the retrieval is examined through diagrams as shown in Figures 6 and 7. Similar to Taylor diagrams [*Taylor*, 2001] that are widely used to evaluate model performance and also skill-bias diagrams [*Hogan and Mason*, 2011], we exploit a relationship between the RMSE, standard deviation, and bias of the retrieval with respect to the truth so that they can be plotted on the same chart. Given that θ is our retrieval of the truth, the following holds:

$$\mathrm{MSE}(\theta) = \mathrm{Var}(\theta) + (\mathrm{Bias}(\theta))^2, \quad (14)$$

where MSE is the mean squared error and Var is the variance. Therefore, if the bias is plotted against the standard deviation of the retrieval, using Pythagoras' rule, lines of equal RMSE emanate from a "perfect retrieval" at the origin. Importantly, this diagram shows how much of the RMSE is attributable to noise (the standard deviation) rather than bias.

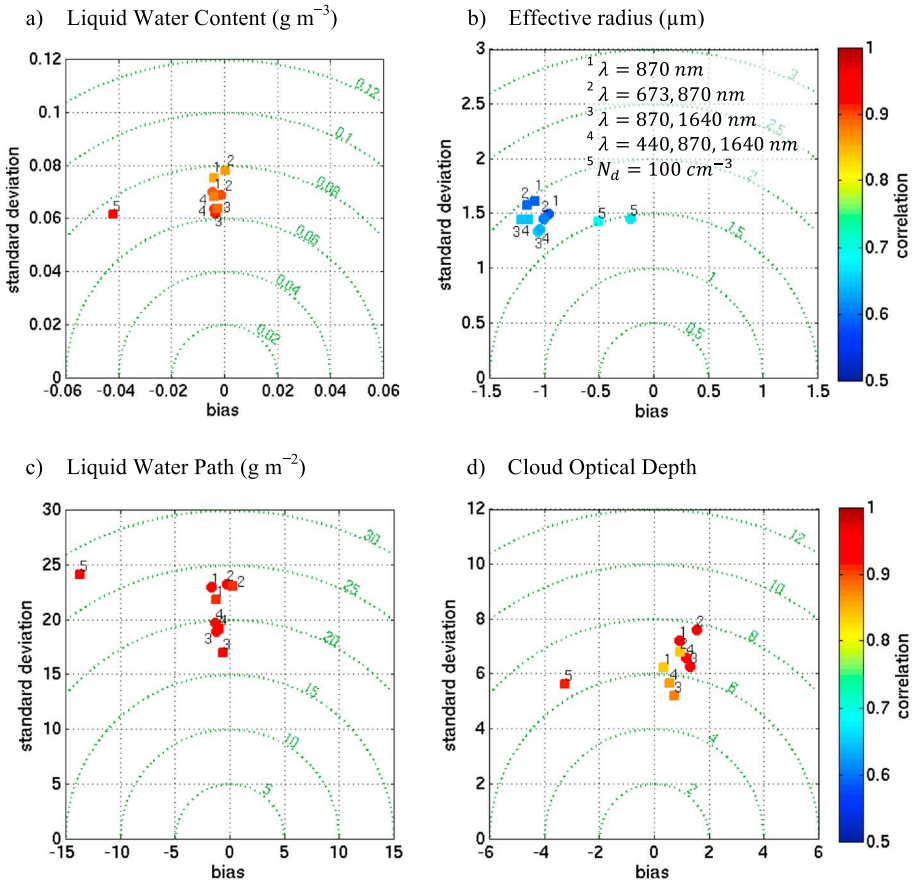

Figure 6. Markers indicating errors in retrieved microphysical properties for different radiance channels, except marker 5 that is for a fixed cloud droplet number concentration. Standard deviation, bias, RMSE (green contours), and correlation (marker color) of the retrieval with respect to the truth are shown for (a) LWC, (b) effective radius, (c) LWP, and (d) optical depth. Markers for the supercolumns only and whole domain are plotted as circles and squares, respectively. The plotted circle with label 5 for Figure 6a has a bias of -0.065 g m^{-3} and standard deviation 0.082 g m^{-3}. Similarly, the plotted circle with label 5 for Figure 6c has bias -16.9 g m^{-2} and standard deviation 30.2 g m^{-2} and Figure 6d has bias -6.6 and standard deviation 4.5.

3.3.1. Effect of Choice of Radiance Wavelength

Ideally, a retrieval that exploits a hyperspectral instrument such as the SAS-Ze would use all the available wavelengths. This would give the best estimate of the state and minimize the uncertainty from observational errors, assuming errors at each wavelength were unbiased and uncorrelated. However, the use of any additional wavelength increases the computational cost of forward modeling the radiances. Further, radiances at certain wavelengths may be more susceptible to biases or loss of information—for example, scattering from aerosols will be greater at shorter wavelengths, so the forward model for radiance at these wavelengths would need to include precise aerosol properties. A careful choice of wavelengths is therefore necessary.

We have examined four different wavelength configurations labeled 1–4 in Figure 6 using the same LES snapshot as previously described, with the aim of understanding if any particular wavelengths are crucial. The first configuration uses just 870 nm, a nonabsorbing wavelength. The second mimics observations from a 2NFOV, which has two nonabsorbing wavelengths at 673 and 870 nm. The third has one nonabsorbing and one absorbing wavelength at 870 and 1640 nm, respectively. Finally, the fourth mimics the SAS-Ze with an additional 440 nm wavelength (nonabsorbing). As a benchmark, we also test a configuration with no radiances and N_d is kept constant at 100 cm^{-3}, which has label 5. In this configuration, no ensemble retrieval is performed since Z can be directly converted to LWC and r_e using equations (2) and (4).

Figure 6 shows retrieval errors in LWC, LWP, r_e, and τ. The lack of radiance constraints in configuration 5 means that all supercolumns, and therefore the entire domain, will have the same N_d as the prior guess. This leads to

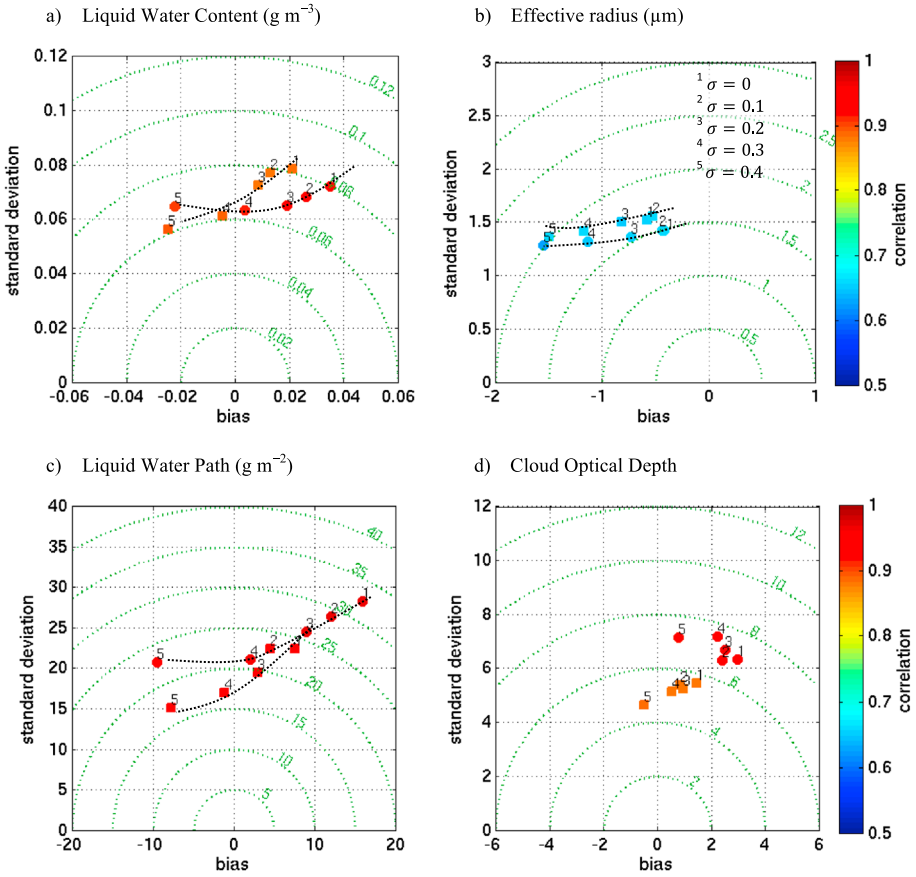

Figure 7. Same as Figure 6 but for different shape parameters σ. The black dotted lines show the response of the error to a change in σ.

a large bias and RMSE for LWC, LWP, and τ, although interestingly it happens to improve the retrieval of r_e. The improvement in r_e, but a degradation of LWC, suggests that the strong constraint of Z on r_e (see equation (4)) forces the retrieval to compromise between correct LWC and correct r_e when N_d is constrained by radiances.

The strong constraint of Z on r_e makes results in Figure 6 somewhat surprising in two aspects. First, comparisons between configurations 1 and 2 suggest the retrievals are insensitive to the additional nonabsorbing wavelength at 673 nm. While wavelengths in configuration 2 are necessary to provide a sufficient surface albedo contrast for methods that use zenith radiances only to reduce retrieval ambiguity [*Chiu et al.*, 2006], the finding in Figure 6 suggests that our new method does not require any particular spectral contrast in surface albedo. Second, comparisons between configurations 1 and 3 suggest that retrievals are improved by the additional absorbing wavelength at 1640 nm. This additional wavelength reduces the RMSE of LWP and τ by 5 g m^{-2} and 1, respectively, and has a negligible impact on r_e. While 1640 nm is the primary wavelength that provides information on cloud droplet size for methods that use zenith radiances only, its impact in our retrieval is overwhelmed by the strong constraint from radar reflectivity. However, we did find that it helped to keep the retrieval stable and reduce noise in N_d. Similar to the comparison between configurations 1 and 2, configuration 4 with the additional 440 nm wavelength has comparable retrieval errors to those in configuration 3.

In short, these findings show that the retrievals are somewhat improved by the inclusion of both an absorbing and a nonabsorbing wavelength but are insensitive to any further additional wavelengths. Results also indicate that the constraint from zenith radiances is mainly on τ, while the constraint from Z is mainly on cloud droplet size and LWC.

3.3.2. Effect of Shape Parameter in Cloud Droplet Size Distribution

In our retrieval we assume that the shape parameter σ of the lognormal droplet distribution is constant. In reality, σ varies both horizontally and vertically due to variability in cloud condensation nuclei, vertical

velocity, microphysical processes, and other atmospheric processes such as entrainment-mixing. This section assesses the sensitivity of retrieved cloud properties to assuming a constant shape parameter.

Figure 7 shows the retrieval performance for the same LES snapshot but using shape parameters ranging from 0 to 0.4. Overall, τ appears less sensitive to the shape parameter (Figure 7d) because radiances directly depend on optical depth, but increasing σ decreases the retrieved mean r_e, LWC, and LWP (as shown in Figures 7a–7c), which can be explained as follows. By combining equations (2)–(4) and ignoring the attenuation term in equation (4) for simplicity, we can rewrite τ as follows:

$$\tau = 2\pi \int_{H_B}^{H_T} Z^{\frac{1}{3}} N_d^{\frac{2}{3}} \exp\left(-4\sigma^2\right) dh. \tag{15}$$

For a given Z and τ, equation (15) indicates that an increase in σ increases N_d, which decreases r_e based on equation (4). Additionally, equation (3) indicates that if r_e decreases, LWC also decreases for a given τ, which is consistent with Figure 7.

Another interesting finding in Figure 7 is that the minimum in bias and RMSE for LWC and LWP occurs when the shape parameter is around 0.3, matching the value derived earlier from the truth. We can use the standard deviation in observed shape parameter of 0.13 found in *Miles et al*. [2000] to estimate a typical range of error for using a shape parameter that differs from the mean. For example, if the shape parameter were chosen in the range 0.17–0.43, Figure 7a suggests that the bias in LWC would be between 0.03 and $-0.03\ \mathrm{g\,m^{-3}}$ (±25% of the domain average; see Table 2) and a maximum RMSE of $0.08\ \mathrm{g\,m^{-3}}$, whereas the retrieval that used the "true" shape parameter gave a bias $< 0.01\ \mathrm{g\,m^{-3}}$ and $< 0.06\ \mathrm{g\,m^{-3}}$ RMSE.

4. Case Study With Real Data

Two cases were chosen to demonstrate our retrieval method using ARM Mobile Facility data at the Azores during November 2009. Potential cases were restricted to daytime, nondrizzling low clouds. At the time, the WSACR (W band SACR) CWRHI scans were performed at a fixed azimuth; to get the best 3-D gridded estimates, we were also restricted to times when the wind direction was approximately perpendicular to these scans. As a result, we selected a relatively homogeneous stratocumulus (Sc) case that later transitioned to a cumulus (Cu) case on 21 November; both Sc and Cu were analyzed. Surface pressure charts confirm a northwesterly airflow with a long fetch across the Atlantic Ocean. We used the WSACR as this was the only radar available. As the field site did not have a SAS-Ze, we used radiances from the 2NFOV.

4.1. Retrieval Configuration

For both cases, we select the same configuration that was used in the synthetic data experiments given in Table 1, except the first guess for N_d is reduced to $50\ \mathrm{cm^{-3}}$ as we expect the aerosol loading to be less than that in the polluted LES case. In spite of this, we found that changing the first guess by a factor of 2 did not affect the retrieved N_d by more than 5%. Additionally, we use a buffer zone of 2500 m to account for the higher ~60° SZA seen in both cases. To match the observed clear-sky radiance, a layer of sulfate aerosol is added to both cases with particle effective radius of 0.1 μm and $10^{-5}\ \mathrm{g\,m^{-3}}$ density in a 1 km layer from the surface. These values are ad hoc and would ideally use estimates from an independent retrieval; changing the aerosol density by a factor of 2 slightly affected the retrieved N_d up to 5%. We make no attempt to model aerosol hygroscopic growth in the vicinity of clouds as in *Charlson et al*. [2007] or *Schmidt et al*. [2009] but expect this effect to be small in the relatively clean aerosol conditions in the Azores.

For each case we use an average wind speed from cloud base to cloud top obtained from a collocated 915 MHz wind profiler retrieval, allowing the temporal radiance and radar data to be mapped to the spatial grid. In both cases, the wind speed was approximately $10\ \mathrm{m\,s^{-1}}$; therefore, to yield a 50 m spatial resolution, the 1 s radiance measurements are linearly averaged over a 5 s time period. Corrections for attenuation in the radar reflectivity in equation (4) are approximated using $k_l = 4.341\ \mathrm{dB\ km^{-1}\ (g\,m^{-3})^{-1}}$, assuming a temperature of 10°C, and the total scattering cross section is small compared to the absorption cross section [*Doviak and Zrnic*, 1993, pp., 43], and $\alpha_f = 0.6358\ \mathrm{dB\ km^{-1}}$, using the line-by-line model of *Liebe* [1985] with the same temperature of 10°C and a saturated atmosphere at 1013 hPa.

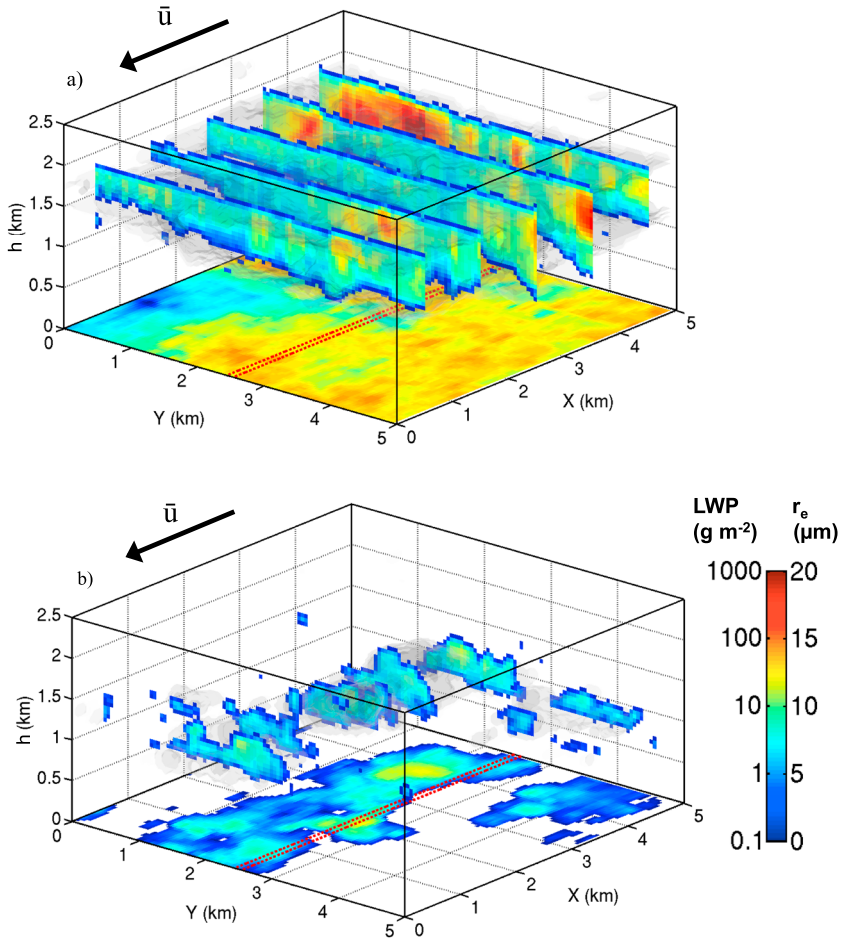

Figure 8. Retrieved cloud fields for (a) stratocumulus case and (b) cumulus case, with 3-D LWC plotted as grey isosurfaces, slices of 3-D effective radius plotted along the *Y* axis and LWP plotted at the surface. The mean wind ($\bar{u}$) direction is shown by the black arrow, while the track of radiances along $Y = 2.5$ km is shown by the red dashed line.

4.2. Retrieval Results

The retrieved 3-D microphysical properties and cloud structure for these two cases are shown in Figure 8, and average microphysical properties are summarized in Table 3. The track of radiances for both cases is along $Y = 2.5$ km, with the clouds passing along the *X* axis from positive to negative. Overall, the domain average N_d, LWP, and r_e are higher for the Sc case than the Cu case. The τ is 3 times greater in the Sc case, but the variability in τ, as a percentage of the mean, is greater in the Cu case.

Figure 9 shows a time series of the observations and retrieved cloud properties for the Sc case directly above the site (i.e., the cross section along $Y = 2.5$ km). The observed radar reflectivity suggests that precipitation is mainly absent and cloud geometric thickness varies between 400 m and 800 m. Toward the end of the time series the stratocumulus is beginning to be coupled with cumulus, as indicated by an area of higher reflectivity underneath the main cloud layer.

Retrieved N_d in Figure 9b generally varies between 50 and 200 cm^{-3}. These values are comfortably in the expected range for stratocumulus in a maritime airmass [*Miles et al*., 2000] and within the variability reported by *Wang et al*. [2009]. Compared to independent LWP retrievals from microwave radiometer (MWR) measurements (MWRRET [*Turner et al*., 2007a]), the retrieval shows good agreement (Figure 9c) with a mean difference of 1 g m^{-2} and root-mean-square difference (RMSD) of 20 g m^{-2}, although the uncertainty of MWRRET is typically 20–30 gm^{-2}. Additionally, the retrieved τ also shows good agreement with those from two-channel zenith radiances only [*Chiu et al*., 2006], with a mean difference of 2.6 and RMSD of 6.5. The observed radiances in Figure 9e are negatively correlated with retrieved τ in Figure 9d, which is expected

Table 3. Mean and Standard Deviation (Std) of Retrieved Microphysical Properties Over Cloudy Regions[a] for a Stratocumulus (Sc) and a Cumulus (Cu) Case From the ARM Mobile Facility Deployment at the Azores on 21 November 2009

	Sc[b]		Cu[c]	
Cloud Property	Mean	Std	Mean	Std
Cloud droplet number concentration N_d (cm^{-3})	69.6	39.2	40.4	32.3
Effective radius r_e (μm)	7.9	3.1	5.8	1.9
Liquid water content ($g\,m^{-3}$)	0.096	0.070	0.028	0.022
Liquid water path ($g\,m^{-2}$)	63.0	26.7	13.5	10.9
Cloud optical depth	12.2	6.0	4.4	3.0
Cloud fraction	1	-	0.24	-

[a]Defined as cloudy voxels greater than 0.01 $g\,m^{-3}$ and columns with LWP greater than 5 $g\,m^{-2}$.
[b]11:25–11:35 UTC.
[c]14:10–14:20 UTC.

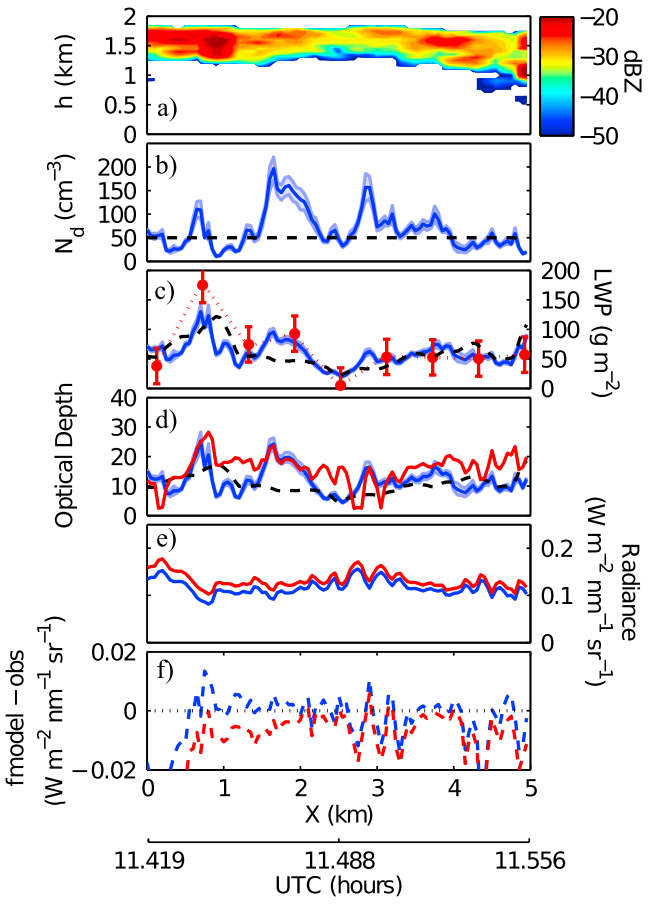

Figure 9. Observations and retrieved cloud properties along the track of radiances ($Y = 2.5$ km) of the stratocumulus case shown in Figure 8. (a) Observed radar reflectivity; (b) retrieved droplet number concentration (dark blue); (c) retrieved liquid water path (dark blue) and MWRRET LWP (red) plotted with ±30 $g\,m^{-2}$ error bars; (d) retrieved cloud optical depth (dark blue), 2NFOV retrieved optical depth (red); (e) observed zenith radiance (673 nm blue line; 870 nm red line); and (f) difference between forward modeled radiances and observations (673 nm blue dashed line; 870 nm red dashed line). The black dashed line in Figures 9b–9d shows the retrieval using the first guess of N_d = 50 cm^{-3}.

in an optically thick overcast cloud field where 3-D effects are less pronounced. Finally, the small differences between the forward modeled radiances and the observed radiances in Figure 9f give us confidence in the retrieval.

To understand how much improvement has been made through the use of the radiances, we compare our retrievals with those calculated from equations (2)–(4) using a climatological N_d of 50 cm^{-3}. As shown by black dashed lines in Figure 9, a reasonable agreement with the MWRRET and radar-only retrieval is found, but some LWP retrievals notably fall outside the uncertainty of the MWRRET. The retrieved average LWP is 15% less compared to MWRRET (the difference between our retrieval and MWRRET was 2%), and the average cloud optical depth is 35% less compared to the radiance-only retrieval (the difference between our retrieval and the radiance-only retrieval was 20%), suggesting the retrieval from the ensemble method has added skill from the first guess of 50 cm^{-3}.

Similarly, Figure 10 shows results for the Cu case. The low reflectivities and absence of virga again suggest that there is no precipitation. The cloud base is generally at 800 m, but the cloud at $X = 2$ km has a higher cloud base of 1200 m and is probably the remnants of the stratocumulus field from earlier in the day. The domain average N_d is slightly smaller than the Sc case and with a slightly smaller range of 10–150 cm^{-3}.

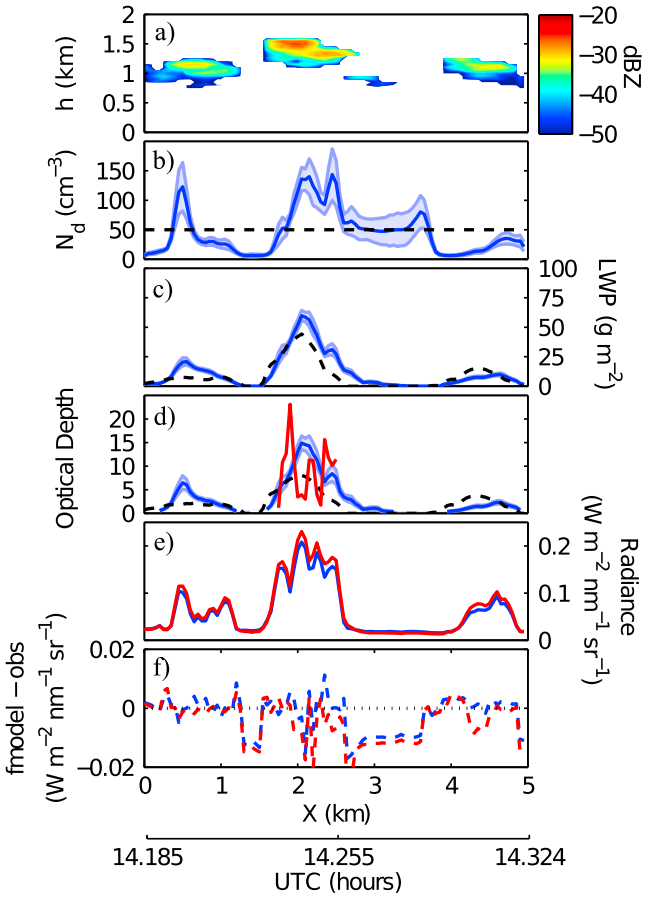

Figure 10. Same as Figure 9 but for the cumulus case shown in Figure 8. Note that the MWR-retrieved LWP is negative and retrievals from two-channel radiances are only physical between 14.24 and 14.26 UTC (hours).

Unfortunately it is difficult to validate the cumulus observations, because retrieval methods based on measurements from either MWR or 2NFOV struggle with the low LWP and heterogeneity that the cumulus presents. Nevertheless, the retrieved τ and 2NFOV τ for the larger cloud in the middle agree in overall magnitude, whereas the optical depth retrieved using a climatological N_d of 50 cm^{-3} is lower. For the smaller clouds at the beginning and end of the time series the 2NFOV retrieval gives an unphysical retrieval due to the so-called "clear-sky contamination" problem (where the field of view is only partially filled with cloud) identified in *Chiu et al.* [2006]. By combining radiances with radar reflectivity, our new method helps resolve this issue. We can also compare the retrieval with in situ measurements of similar clouds; the mean LWC of 0.03 g m^{-3} is reasonable for nonprecipitating shallow cumulus. At around $X = 3$ km the retrieval has a large uncertainty in N_d and the forward modeled radiances are systematically underestimated. Here the radar reflectivity is very low, and the underestimation in radiances could be due to haze particles at cloud edge that are not detectable by the radar.

5. Discussion

In this section we discuss issues related to radar sensitivity and computational cost for future potential improvements. Radar sensitivity limits both the domain size of the retrieval and the ability to detect cloud edges. The current implementation was limited to 5 km × 5 km × 5 km because of the sensitivity of the W band scanning cloud radar; a large fraction of cloud would not be detected beyond this domain. For example, for the scanning radar used here, the minimum detectable reflectivity at 5 km is estimated at −27.5 dB*Z*. At 10 km this increases to −22.5 dB*Z*, which would miss nearly all the clouds in both stratocumulus and cumulus cases described in the previous section. Increasing the sensitivity of the SACRs is an ARM priority and would reduce the chance of missing clouds and hence reduce the retrieval uncertainty.

However, cloud edges are likely to be missed even within the limited domain, leading to errors in the retrieval. Examples of the effects of radar sensitivity on retrieved 3-D cloud microphysical properties are given in *Fielding et al.* [2013]. Missing a horizontal cloud edge is particularly troublesome as it is likely that no cloud would be retrieved in the whole column. This could then affect the retrieval of neighboring columns where cloud is detected, through knock-on errors in the 3-D radiative transfer modeling of radiances. For example, a cloudy pixel neighboring a missed edge might be brighter in the forward model (due to illumination) than in reality. A potential solution could be that when cloud edges are detected in the zenith radiances but not by the radar, artificial observations of radar reflectivity are added to the edges of nearby clouds.

Additionally, using 3-D radiative transfer as a forward model is computationally expensive, driving many of the choices for our implementation of the retrieval. For example, when forward modeling radiances, we need to use a buffer zone that surrounds the retrieved supercolumn to ensure that nearby clouds are well

represented. With unlimited computer resources, one could set the buffer zone to be as large as possible. However, there would be a point where the benefit of increasing the buffer zone further would be limited by the sensitivity of the radar to observe more distant clouds.

Another adjustable parameter, the supercolumn size (the size of the domain where cloud properties are retrieved directly by the ensemble method), is largely restricted by the influence of the cloud field on zenith radiances. Increasing the supercolumn size beyond a few hundred meters potentially introduces instability in the retrieval. For a given observed radiance, there could be many different realizations of the cloud field that give the same forward modeled radiance, particularly for lower sun elevation angles. For larger supercolumns we often found the retrieved variables would oscillate, creating unrealistic yet technically correct solutions. One way around this problem is to apply a smoothness constraint to the problem. This can be implemented in the method by creating correlations between the state variables when initializing the ensembles. Subsequent iterations retain the correlation, effectively smoothing the solution. Also, as this smoothing reduces the degrees of freedom of the problem, the number of ensemble members required for an accurate solution is reduced.

6. Summary and Conclusions

Using ground-based observations, we introduced for the first time a new cloud retrieval method that provides 2-D fields of N_d and 3-D fields of LWC and r_e for nonprecipitating warm liquid water clouds. The method exploits not only synergetic measurements of scanning cloud radar and shortwave spectral radiances but also a novel ensemble method that incorporates radiance constraints using 3-D radiative transfer code, which is extremely difficult for other retrieval techniques (e.g., variational methods). Importantly, the constraints from spectral radiances help our retrievals achieve consistency between cloud microphysical and optical properties and between shortwave and microwave spectral regions. Since our retrieval is independent of LWP retrievals from MWR measurements, it greatly enhances ground-based LWC observations and can serve as an invaluable evaluation data set.

The retrieval performance was first evaluated using synthetic measurements generated from a LES shallow cumulus case, whose small cloud sizes and highly inhomogeneous features pose a great challenge to retrieval methods. In general, the true LWP in this case was an average of 37 g m^{-2} and did not exceed 400 g m^{-2}. The domain size in the horizontal was set around 6.4 km at 50 m resolution, based on the scan speed and the sensitivity of typical cloud radars. Synthetic measurements of radar reflectivity and zenith spectral radiances were generated to mimic ARM SACR and shortwave radiometer observations (e.g., SWS-Ze and 2NFOV), respectively. Given the uncertainty in the observations, the retrieval uncertainty in the supercolumns (a subdomain directly above the observation site) of LWC is 20% and r_e 6%. Without the radiance observation at 1640 nm, an absorbing wavelength, the RMSE in LWC increased by 10–20% for retrievals that only use nonabsorbing wavelengths.

The retrieval performance was also evaluated using real data from the ARM Mobile Facility deployment at the Azores for stratocumulus and cumulus clouds. In the stratocumulus case, retrieved LWP shows good agreement with that from independent MWR measurements, with 1 g m^{-2} bias and RMSD of 20 g m^{-2}. Additionally, the retrieved τ shows good agreement with 2NFOV τ, with a difference of 2.6 and RMSD of 6.5. Unfortunately in the cumulus case, the retrievals are difficult to compare with those from MWR and 2NFOV as they are either unphysical or unavailable for this broken-cloud case with low LWP. Future observations from more scanning radars, SWS-Ze, and a three-channel MWR that has higher sensitivity to low LWP clouds will help make robust evaluations of the retrievals.

The assumed unimodal lognormal droplet distribution in the retrieval is not suitable for drizzling cloud. However, the flexible framework should allow for adaptations to retrieve cloud properties in precipitating cloud if additional information to separate the drizzle and cloud contributions to radar reflectivity is included. Possible sources of information include lidar, dual-wavelength radar, or Doppler spectra analysis, which is an ongoing area of research. The framework would also allow the addition of further radiance observations from scanning spectrometers [e.g., *Kassianov et al*., 2012] or nonscanning multidirectional spectroradiometers [e.g., *Riechelmann et al*., 2013] to enhance radiance constraints from more directions, which could potentially improve overall retrievals.

Acknowledgments

ARM data is made available online through the U.S. Department of Energy as part of the Atmospheric Radiation Measurement Program at http://www.archive.arm.gov. This research was supported by the Office of Science (BER), U.S. Department of Energy (DOE) under grant DE-SC0007233. G.F. acknowledges DOE's Office of Science (BER) and NOAA's Climate Goal for support. We would like to thank the Department of Meteorology, University of Reading, for hosting G.F.'s visit during summer 2013, and Javier Amezcua and Shuhua Chen for insightful discussion on the ensemble Kalman filter.

References

Ackerman, T. P., and G. M. Stokes (2003), The Atmospheric Radiation Measurement program, *Phys. Today*, *56*(1), 38–44, doi:10.1063/1.1554135.

Austin, R. T., and G. L. Stephens (2001), Retrieval of stratus cloud microphysical parameters using millimeter-wave radar and visible optical depth in preparation for CloudSat—1. Algorithm formulation, *J. Geophys. Res.*, *106*(D22), 28,233–28,242, doi:10.1029/2000JD000293.

Barker, H. W., M. P. Jerg, T. Wehr, S. Kato, D. P. Donovan, and R. J. Hogan (2011), A 3D cloud-construction algorithm for the EarthCARE satellite mission, *Q. J. R. Meteorol. Soc.*, *137*(657), 1042–1058, doi:10.1002/Qj.824.

Cahalan, R. F., W. Ridgway, W. J. Wiscombe, S. Gollmer, and Harshvardhan (1994), Independent pixel and Monte-Carlo estimates of stratocumulus albedo, *J. Atmos. Sci.*, *51*(24), 3776–3790, doi:10.1175/1520-0469(1994)051<3776:Ipamce>2.0.Co;2.

Charlson, R. J., A. S. Ackerman, F. A. M. Bender, T. L. Anderson, and Z. Liu (2007), On the climate forcing consequences of the albedo continuum between cloudy and clear air, *Tellus B*, *59*(4), 715–727, doi:10.1111/j.1600-0889.2007.00297.x.

Chiu, J. C., A. Marshak, Y. Knyazikhin, W. J. Wiscombe, H. W. Barker, J. C. Barnard, and Y. Luo (2006), Remote sensing of cloud properties using ground-based measurements of zenith radiance, *J. Geophys. Res.*, *111*, D16201, doi:10.1029/2005JD006843.

Chiu, J. C., A. Marshak, C. H. Huang, T. Varnai, R. J. Hogan, D. M. Giles, B. N. Holben, E. J. O'Connor, Y. Knyazikhin, and W. J. Wiscombe (2012), Cloud droplet size and liquid water path retrievals from zenith radiance measurements: Examples from the atmospheric radiation measurement program and the aerosol robotic network, *Atmos. Chem. Phys.*, *12*(21), 10,313–10,329, doi:10.5194/acp-12-10313-2012.

Dong, X. Q., and G. G. Mace (2003), Profiles of low-level stratus cloud microphysics deduced from ground-based measurements, *J. Atmos. Oceanic Technol.*, *20*(1), 42–53, doi:10.1175/1520-0426(2003)020<0042:Pollsc>2.0.Co;2.

Doviak, R. J., and D. S. Zrnic (1993), *Doppler Radar and Weather Observations*, 2nd ed., Academic Press, San Diego, Calif.

Evans, K. F. (1998), The spherical harmonics discrete ordinate method for three-dimensional atmospheric radiative transfer, *J. Atmos. Sci.*, *55*(3), 429–446, doi:10.1175/1520-0469(1998)055<0429:Tshdom>2.0.Co;2.

Evensen, G. (2003), The ensemble Kalman filter: Theoretical formulation and practical implementation, *Ocean Dyn.*, *53*(4), 343–367.

Evensen, G., and P. J. VanLeeuwen (1996), Assimilation of Geosat altimeter data for the Agulhas Current using the ensemble Kalman filter with a quasigeostrophic model, *Mon. Weather Rev.*, *124*(1), 85–96, doi:10.1175/1520-0493(1996)124<0085:Aogadf>2.0.Co;2.

Fielding, M. D., J. C. Chiu, R. J. Hogan, and G. Feingold (2013), 3D cloud reconstructions: Evaluation of scanning radar scan strategy with a view to surface shortwave radiation closure, *J. Geophys. Res. Atmos*, *118*, 9153–9167, doi:10.1002/Jgrd.50614.

Frisch, A. S., C. W. Fairall, and J. B. Snider (1995), Measurement of stratus cloud and drizzle parameters in ASTEX with a K-alpha-band Doppler radar and a microwave radiometer, *J. Atmos. Sci.*, *52*(16), 2788–2799, doi:10.1175/1520-0469(1995)052<2788:Moscad>2.0.Co;2.

Frisch, A. S., G. Feingold, C. W. Fairall, T. Uttal, and J. B. Snider (1998), On cloud radar and microwave radiometer measurements of stratus cloud liquid water profiles, *J. Geophys. Res.*, *103*(D18), 23,195–23,197, doi:10.1029/98JD01827.

Gillijns, S., O. B. Mendoza, J. Chandrasekar, B. L. R. De Moor, D. S. Bernstein, and A. Ridley (2006), What is the ensemble Kalman filter and how well does it work?, *Proc. Am. Control Conf.*, *1–12*, 4448–4453, doi:10.1109/Acc.2006.1657419.

Grecu, M., and W. S. Olson (2008), Precipitating snow retrievals from combined airborne cloud radar and millimeter-wave radiometer observations, *J. Appl. Meteorol. Climatol.*, *47*(6), 1634–1650, doi:10.1175/2007jamc1728.1.

Hartmann, D. L., M. E. Ockertbell, and M. L. Michelsen (1992), The effect of cloud type on earths energy-balance—Global analysis, *J. Clim.*, *5*(11), 1281–1304, doi:10.1175/1520-0442(1992)005<1281:Teocto>2.0.Co;2.

Hogan, R. J. (2007), A variational scheme for retrieving rainfall rate and hail reflectivity fraction from polarization radar, *J. Appl. Meteorol. Climatol.*, *46*(10), 1544–1564, doi:10.1175/Jam2550.1.

Hogan, R. J., and I. B. Mason (2011), Deterministic forecasts of binary events, in *Forecast Verification: A Practitioner's Guide in Atmospheric Science*, 2nd ed., edited by I. T. Jolliffe and D. B. Stephenson, John Wiley Ltd., Chichester, U. K., doi:10.1002/9781119960003.ch3.

Hogan, R. J., and J. K. P. Shonk (2013), Incorporating the effects of 3D radiative transfer in the presence of clouds into two-stream multilayer radiation schemes, *J. Atmos. Sci.*, *70*(2), 708–724, doi:10.1175/Jas-D-12-041.1.

Hogan, R. J., N. Gaussiat, and A. J. Illingworth (2005), Stratocumulus liquid water content from dual-wavelength radar, *J. Atmos. Oceanic Technol.*, *22*(8), 1207–1218, doi:10.1175/Jtech1768.1.

Holben, B. N., et al. (1998), AERONET—A federated instrument network and data archive for aerosol characterization, *Remote Sens. Environ.*, *66*(1), 1–16, doi:10.1016/S0034-4257(98)00031-5.

Huang, D., K. Johnson, Y. Liu, and W. Wiscombe (2009), High resolution retrieval of liquid water vertical distributions using collocated Ka-band and W-band cloud radars, *Geophys. Res. Lett.*, *36*, L24807, doi:10.1029/2009GL041364.

Ide, K., P. Courtier, M. Ghil, and A. C. Lorenc (1997), Unified notation for data assimilation: Operational, sequential and variational, *J. Meteorol. Soc. Jpn.*, *75*(1B), 181–189.

Iglesias, M. A., K. J. H. Law, and A. M. Stuart (2013), Ensemble Kalman methods for inverse problems, *Inverse Probl.*, *29*(4), doi:10.1088/0266-5611/29/4/045001.

Illingworth, A. J., et al. (2007), Cloudnet—Continuous evaluation of cloud profiles in seven operational models using ground-based observations, *Bull. Am. Meteorol. Soc.*, *88*(6), 883–898, doi:10.1175/Bams-88-6-883.

Jiang, H. L., G. Feingold, and I. Koren (2009), Effect of aerosol on trade cumulus cloud morphology, *J. Geophys. Res.*, *114*, D11209, doi:10.1029/2009JD011750.

Kassianov, E., C. Flynn, J. Redemann, B. Schmid, P. B. Russell, and A. Sinyuk (2012), Initial assessment of the Spectrometer for Sky-Scanning, Sun-Tracking Atmospheric Research (4STAR)-based aerosol retrieval: Sensitivity study, *Atmos.-Basel*, *3*(4), 495–521, doi:10.3390/Atmos3040495.

Kollias, P., N. Bharadwaj, K. Widener, I. Jo, and K. Johnson (2014), Scanning ARM cloud radars. Part I: Operational sampling strategies, *J. Atmos. Oceanic Technol.*, *31*, 569–582, doi:10.1175/JTECH-D-13-00044.1.

Liebe, H. J. (1985), An updated model for millimeter wave-propagation in moist air, *Radio Sci.*, *20*(5), 1069–1089, doi:10.1029/RS020i005p01069.

Lohnert, U., S. Crewell, C. Simmer, and A. Macke (2001), Profiling cloud liquid water by combining active and passive microwave measurements with cloud model statistics, *J. Atmos. Oceanic Technol.*, *18*(8), 1354–1366, doi:10.1175/1520-0426(2001)018<1354:Pclwbc>2.0.Co;2.

Marshak, A., Y. Knyazikhin, K. D. Evans, and W. J. Wiscombe (2004), The "RED versus NIR" plane to retrieve broken-cloud optical depth from ground-based measurements, *J. Atmos. Sci.*, *61*(15), 1911–1925, doi:10.1175/1520-0469(2004)061<1911:Trvnpt>2.0.Co;2.

McBride, P. J., K. S. Schmidt, P. Pilewskie, A. S. Kittelman, and D. E. Wolfe (2011), A spectral method for retrieving cloud optical thickness and effective radius from surface-based transmittance measurements, *Atmos. Chem. Phys.*, *11*(14), 7235–7252, doi:10.5194/acp-11-7235-2011.

McFarlane, S. A., and K. F. Evans (2004), Clouds and shortwave fluxes at Nauru. Part I: Retrieved cloud properties, *J. Atmos. Sci.*, *61*(6), 733–744, doi:10.1175/1520-0469(2004)061<0733:Casfan>2.0.Co;2.

McFarlane, S. A., K. F. Evans, and A. S. Ackerman (2002), A Bayesian algorithm for the retrieval of liquid water cloud properties from microwave radiometer and millimeter radar data, *J. Geophys. Res.*, *107*(D16), 4317, doi:10.1029/2001JD001011.

Miles, N. L., J. Verlinde, and E. E. Clothiaux (2000), Cloud droplet size distributions in low-level stratiform clouds, *J. Atmos. Sci.*, *57*(2), 295–311, doi:10.1175/1520-0469(2000)057<0295:Cdsdil>2.0.Co;2.

Oreopoulos, L., and S. Platnick (2008), Radiative susceptibility of cloudy atmospheres to droplet number perturbations: 2. Global analysis from MODIS, *J. Geophys. Res.*, *113*, D14S21, doi:10.1029/2007JD009655.

Pincus, R., C. Hannay, and K. F. Evans (2005), The accuracy of determining three-dimensional radiative transfer effects in cumulus clouds using ground-based profiling instruments, *J. Atmos. Sci.*, *62*(7), 2284–2293, doi:10.1175/Jas3464.1.

Qian, Y., C. N. Long, H. Wang, J. M. Comstock, S. A. McFarlane, and S. Xie (2012), Evaluation of cloud fraction and its radiative effect simulated by IPCC AR4 global models against ARM surface observations, *Atmos. Chem. Phys.*, *12*(4), 1785–1810, doi:10.5194/acp-12-1785-2012.

Randall, D. A., et al. (2007), Climate models and their evaluation, in *Climate Change 2007: The Physical Science Basis. Contribution of Working Group I to the Fourth Assessment Report of the Intergovernmental Panel on Climate Change*, edited by S. Solomon et al., pp. 589–662, Cambridge Univ. Press, Cambridge, U. K., and New York.

Rémillard, J., P. Kollias, and W. Szyrmer (2013), Radar-radiometer retrievals of cloud number concentration and dispersion parameter in nondrizzling marine stratocumulus, *Atmos. Meas. Tech.*, *6*(7), 1817–1828, doi:10.5194/amt-6-1817-2013.

Riechelmann, S., M. Schrempf, and G. Seckmeyer (2013), Simultaneous measurement of spectral sky radiance by a non-scanning multidirectional spectroradiometer (MUDIS), *Meas. Sci. Technol.*, *24*(12), doi:10.1088/0957-0233/24/12/125501.

Schaaf, C. B., et al. (2002), First operational BRDF, albedo nadir reflectance products from MODIS, *Remote Sens. Environ.*, *83*(1–2), 135–148, doi:10.1016/S0034-4257(02)00091-3.

Schmidt, K. S., G. Feingold, P. Pilewskie, H. Jiang, O. Coddington, and M. Wendisch (2009), Irradiance in polluted cumulus fields: Measured and modeled cloud-aerosol effects, *Geophys. Res. Lett.*, *36*, L07804, doi:10.1029/2008GL036848.

Taylor, K. E. (2001), Summarizing multiple aspects of model performance in a single diagram, *J. Geophys. Res.*, *106*(D7), 7183–7192, doi:10.1029/2000JD900719.

Turner, D. D., S. A. Clough, J. C. Lijegren, E. E. Clothiaux, K. E. Cady-Pereira, and K. L. Gaustad (2007a), Retrieving liquid water path and precipitable water vapor from the atmospheric radiation measurement (ARM) microwave radiometers, *IEEE Trans. Geosci. Remote*, *45*(11), 3680–3690, doi:10.1109/Tgrs.2007.903703.

Turner, D. D., et al. (2007b), Thin liquid water clouds—Their importance and our challenge, *Bull. Am. Meteorol. Soc.*, *88*(2), 177–374, doi:10.1175/Bams-88-2-177.

Wang, J., P. H. Daum, S. S. Yum, Y. Liu, G. I. Senum, M.-L. Lu, J. H. Seinfeld, and H. Jonsson (2009), Observations of marine stratocumulus microphysics and implications for processes controlling droplet spectra: Results from the Marine Stratus/Stratocumulus Experiment, *J. Geophys. Res.*, *114*, D18210, doi:10.1029/2008JD011035.

Wang, P., W. H. Knap, and P. Stammes (2011), Cloudy sky shortwave radiative closure for a Baseline Surface Radiation Network site, *J. Geophys. Res.*, *116*, D08202, doi:10.1029/2010JD015141.

Widener, K., N. Bharadwaj, and K. Johnson (2012), *Scanning ARM Cloud Radar Handbook*, doi:10.2172/1043296.

Yang, S. C., E. Kalnay, and B. Hunt (2012), Handling nonlinearity in an ensemble Kalman filter: Experiments with the three-variable Lorenz model, *Mon. Weather Rev.*, *140*(8), 2628–2646, doi:10.1175/Mwr-D-11-00313.1.